

## Insulating traveling-wave electrophoresis

Raúl Fernández-Mateo <sup>1</sup>, Víctor Calero <sup>2</sup>, Hywel Morgan <sup>1</sup>, Pablo García-Sánchez <sup>2</sup>, and Antonio Ramos <sup>2,\*</sup>

<sup>1</sup>*School of Electronics and Computer Science, University of Southampton, Southampton SO17 1BJ, United Kingdom*

<sup>2</sup>*Departamento de Electrónica y Electromagnetismo, Facultad de Física, Universidad de Sevilla, Avda. Reina Mercedes s/n, 41012 Sevilla, Spain*



(Received 18 April 2023; accepted 29 June 2023; published 24 July 2023)

Traveling-wave electrophoresis (TWE) is a method for transporting charged colloidal particles used in many microfluidic techniques for particle manipulation and fractionation. This method exploits the traveling-wave components of the electric field generated by an array of electrodes subjected to ac voltages with a phase delay between neighboring electrodes. In this article, we propose an alternative way of generating traveling-wave electric fields in microchannels. We apply a rotating electric field around a cylindrical insulating micropillar and the resulting traveling-wave modes induce particle drift around the cylinder. We term this phenomenon insulating traveling-wave electrophoresis (i-TWE) to distinguish it from standard TWE performed with arrays of microelectrodes. We characterized the particle drift experimentally and show a quantitative comparison of the particle velocity with theoretical predictions. Excellent agreement is found when the influence of electro-osmosis on the channel walls is also considered.

DOI: [10.1103/PhysRevE.108.015104](https://doi.org/10.1103/PhysRevE.108.015104)

### I. INTRODUCTION

Electrophoresis is widely used to manipulate and separate charged particles (colloids, molecules) suspended in electrolytes, and capillary electrophoresis [1] is the standard for high-efficiency separation of molecules. Electrophoresis describes the motion of a particle due to the action of an electric field on the electrical double layer (EDL) at the particle-electrolyte interface [2]. When the EDL is thin with respect to the particle size, the electrophoretic velocity of the particle  $\mathbf{u}_{ep}$  is given by the Helmholtz-Smoluchowski formula [3]

$$\mathbf{u}_{ep} = \frac{\varepsilon\zeta}{\eta} \mathbf{E}, \quad (1)$$

where  $\mathbf{E}$  is the applied electric field,  $\varepsilon$  and  $\eta$  are the electrolyte permittivity and viscosity respectively, and  $\zeta$  is the zeta potential. The latter is usually defined as the electrical potential at the inner edge of the diffuse ionic layer surrounding the particle [2].

Recent papers have shown that traveling-wave (TW) electric fields can be used to achieve electrophoretic motion of charged particles with a controlled direction and velocity magnitude, a phenomenon known as traveling-wave electrophoresis (TWE) [4]. TW electric fields are conventionally generated using arrays of microelectrodes connected to oscillating potentials of the same frequency but with a fixed

phase lag between neighboring electrodes [see Fig. 1(a)]. In TWE, there are fundamentally two different modes depending on the relative value of electrophoretic velocity to the phase velocity of the wave, which is  $v = \omega/k$ , where  $\omega$  is the angular frequency of the ac voltage on the electrodes and  $k$  is the wave number of the TW electric field  $k = 2\pi/L$ , where  $L$  is the spatial periodicity [see Fig. 1(a)]. If  $v \leq u_{ep}$ , the particles “surf” the traveling wave and their motion is synchronous, i.e., their velocity is that of the wave phase. However, if the traveling wave is faster ( $v > u_{ep}$ ), the particles cannot follow and migrate by partially following each successive wave crest, this is called asynchronous motion. For this reason, the ratio  $v/u_{ep}$  has been defined as the responsiveness of the particles to the wave [4].

In 2007, Wei [5] proposed the use of TWE for mobility-based particle fractionation inside microfluidic channels. Edwards *et al.* [4] showed good agreement between theory and velocity measurements of TWE experiments in microfluidics. They also showed that chaotic behavior is theoretically expected for intermediate values of the particle mobility. Jo *et al.* [6] used TWE in a microchannel and demonstrated efficient separation of fluorescent dyes and proteins with relatively narrow sample bandwidths.

In this work, we show how TW fields can be created around insulating objects and how these fields can be used to control particle migration in a similar manner to “classical” TWE with microelectrode arrays. We achieve this by applying a rotating electric field around an insulating micropillar placed in a microfluidic chamber, as shown in Fig. 1(b). The rotating electric field is generated by four electrodes placed far from the chamber. This arrangement is simpler than using an array of microelectrodes, which requires a complicated wiring scheme to address each electrode with the appropriate electrical signal. Creation of the traveling-wave electric fields far from the

\*Corresponding author: ramos@us.es

Published by the American Physical Society under the terms of the [Creative Commons Attribution 4.0 International](https://creativecommons.org/licenses/by/4.0/) license. Further distribution of this work must maintain attribution to the author(s) and the published article’s title, journal citation, and DOI.

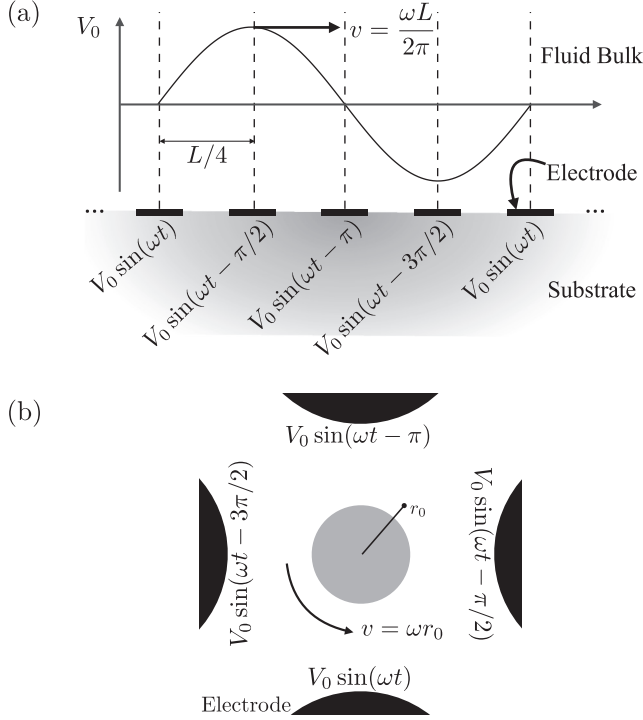


FIG. 1. (a) Diagram showing a classical TWE electrode configuration where an array of electrodes is connected to an oscillating electric potential of the same frequency  $\omega$  but a different phase. This produces an approximate harmonic wave in the fluid bulk with a spatial periodicity  $L$ . (b) Diagram showing the electrode array (in black) and the insulating pillar (in grey) that produces the rotating traveling wave.

electrodes also avoids other undesired effects such as Faradaic reactions [7], which usually cause electrode degradation and modification of liquid conductivity and pH, and the generation of ac electro-osmotic flows on microelectrode in contact with the electrolyte [8].

We use the term insulating traveling-wave electrophoresis (iTWE) to distinguish this approach from the standard TWE with arrays of microelectrodes. In this work, we experimentally measured the velocity of particles undergoing iTWE and performed a quantitative comparison with both numerical simulations and an analytical model that is derived in the limit of high electric field frequency. Excellent agreement is found with experimental data provided that electro-osmosis on the channel walls is included in the model.

## II. THEORY

Consider the application of a harmonic electrical potential with angular frequency  $\omega$  in an electrolyte liquid given by the following expression in polar coordinates  $(r, \theta)$ :

$$\bar{\phi}(\bar{r}, \theta, \bar{t}) = \mathcal{R}e[-E_0 \bar{r} e^{i(\theta - \omega \bar{t})}], \quad (2)$$

where  $E_0$  is a constant,  $\mathcal{R}e[\dots]$  means the real part of the expression between brackets, and the bar indicates a dimensional variable. As shown in the experimental section, an approximation to this electric potential can be achieved using a quadrupolar array of electrodes driven by ac voltages with

a relative phase lag of  $90^\circ$ . The electric field associated with Eq. (2) corresponds to a counterclockwise rotating field within the XY plane and with magnitude  $E_0$ .

If an insulating obstacle is placed within the electrolyte, the electrical current cannot penetrate it and therefore the field lines are distorted around the surface. The zero current condition at the surface  $S$  transforms into the following boundary condition for the potential:  $\mathbf{n} \cdot \nabla \phi|_S = 0$ , where  $\mathbf{n}$  is a unit vector normal to  $S$ . In the case of a cylindrical object of radius  $R$ , with the axis perpendicular to the rotation plane and containing the point  $r = 0$ , the electrical potential in the liquid is

$$\bar{\phi}(\bar{r}, \theta, \bar{t}) = -E_0 \left( \bar{r} + \frac{R^2}{\bar{r}} \right) \mathcal{R}e[e^{i(\theta - \omega \bar{t})}]. \quad (3)$$

For convenience, the potential is scaled by  $E_0 R$ . The length scale is chosen to be the radius of the post  $R$ , and the time scale the inverse of the electric field angular frequency  $1/\omega$ . Using these scaling parameters, the expression Eq. (3) can be rewritten in a nondimensional form as

$$\phi(r, \theta, t) = -\left( r + \frac{1}{r} \right) \mathcal{R}e[e^{i(\theta - t)}] \quad (4)$$

and therefore the electric field is

$$\mathbf{E} = \left( 1 - \frac{1}{r^2} \right) \cos(\theta - t) \hat{r} - \left( 1 + \frac{1}{r^2} \right) \sin(\theta - t) \hat{\theta}. \quad (5)$$

The components of the electric field at a given distance  $r = r_0$  from the center of the pillar can be seen as waves traveling in the angular direction with wavenumber  $k = 1/r_0$ . Thus, the phase velocity of these waves corresponds to  $v = \omega r_0$ . Following on from the description of TWE in the introduction, we expect a synchronous drift for particles with  $u_{ep} \geq \omega r_0$ . In our experiments we used colloidal particles suspended in electrolytes, with  $\zeta \approx -60$  mV and a field magnitude of  $E_0 = 10^4$  V/m. Notice that we are in the linear regime of electrophoresis. Nonlinear effects are reported in experiments with more intense fields and larger particles, as reviewed by A. Khair [9]. The asynchronous regime occurs if  $r > 1.01R$  for the lowest frequency applied ( $f = 13$  Hz). This means that, in practice, the asynchronous regime is to be expected for all experimental conditions. Figure 2(a) shows the asynchronous trajectory of a particle undergoing electrophoretic motion due to this electric field. In this regime, the particle drifts in the angular direction while it oscillates in the radial direction.

In order to develop an analytical expression for the drift velocity, we follow the high-frequency asynchronous (HFA) approximation employed by J.R. Melcher *et al.* [10], where the spatial variables were decomposed into one oscillating component and a time-averaged drift velocity. In our case,

$$r = r_0 + r', \quad \theta = \omega_p t + \theta', \quad (6)$$

where the primed variables denote purely oscillating terms and are assumed to be  $r', \theta' \ll 1$ . That is, the radial component is expected to have small oscillations around a fixed position  $r_0$ , and the angular component is expected to grow linearly over time with a time-averaged angular drift  $\omega_p$  plus small oscillations around this linear growth.

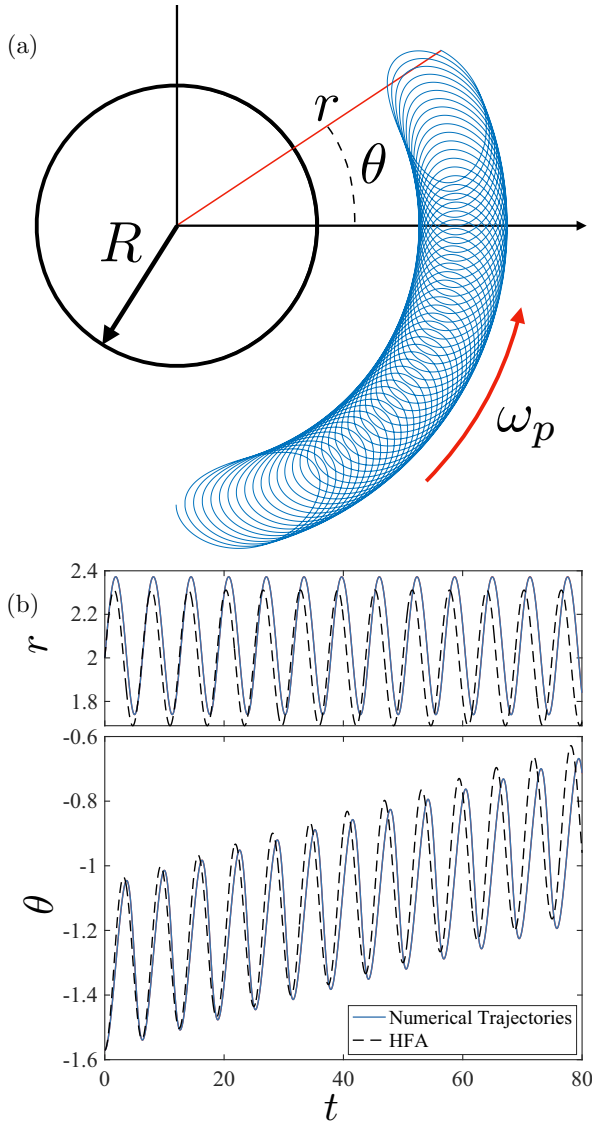


FIG. 2. Analysis of the Rotating TWE system. (a) Sketch of the system showing the trajectory of a single particle ( $\tilde{u} = 0.418$ ,  $r_0 = 2$ ) obtained by direct numerical integration of the equations. The particle describes loops with an overall drift angular velocity  $\omega_p$ . (b) Radial and angular coordinates representing the same case as (a) described by simulation of trajectories (blue) and by the high-frequency asynchronous approximation (HFA, dashed black).

The electrophoretic response of the particles given by Eq. (1) leads to the following nondimensional equations of motion:

$$\frac{dr'}{dt} = \tilde{u} \left( 1 - \frac{1}{(r_0 + r')^2} \right) \cos[\theta' - (1 - \omega_p)t], \quad (7)$$

$$\omega_p + \frac{d\theta'}{dt} = -\tilde{u} \left( \frac{1}{r_0 + r'} + \frac{1}{(r_0 + r')^3} \right) \sin[\theta' - (1 - \omega_p)t], \quad (8)$$

where  $\tilde{u} = \mu E_0 / \omega R$  is the scaled velocity, and  $\mu = \varepsilon \zeta / \eta$  the electrophoretic mobility. Since the oscillating components are much smaller than 1 the equations for  $r'$  and  $\theta'$  can be

written as

$$\frac{dr'}{dt} = \tilde{u} \left( 1 - \frac{1}{r_0^2} \right) \cos[(1 - \omega_p)t], \quad (9)$$

$$\frac{d\theta'}{dt} = \tilde{u} \left( \frac{1}{r_0} + \frac{1}{r_0^3} \right) \sin[(1 - \omega_p)t]. \quad (10)$$

Note that this approximation is valid as long as  $\tilde{u} \ll 1$ . With the expressions for  $r'$  and  $\theta'$ , the time average of Eq. (8) at the lowest order in the expansion gives an expression for the average of the angular drift velocity

$$\begin{aligned} \omega_p = & \tilde{u} \left( \frac{1}{r_0^2} + \frac{3}{r_0^4} \right) \langle r' \sin[(1 - \omega_p)t] \rangle \\ & - \tilde{u} \left( \frac{1}{r_0} + \frac{1}{r_0^3} \right) \langle \theta' \cos[(1 - \omega_p)t] \rangle, \end{aligned} \quad (11)$$

where  $\langle \dots \rangle$  stands for time average. After some algebra, in the limit of  $\omega_p \ll 1$ , we obtain the following expression for the time-averaged drift velocity of the particles around the cylinder:

$$\omega_p = \frac{1}{2} - \sqrt{\frac{1}{4} - \frac{2\tilde{u}^2}{r_0^6}} \approx \frac{2\tilde{u}^2}{r_0^6}. \quad (12)$$

Figure 2 shows a calculation for the case of  $\tilde{u} = 0.418$  and  $r_0 = 2$ . Figures 2(b) and 3 show a comparison between the HFA approximation and numerical simulations using the full electrophoretic velocity corresponding to the field in Eq. (5). In this case, the drift velocity  $\omega_p$  obtained from the HFA approximation differs from the average displacement given by the numerical trajectories by 8%.

Figure 3 shows  $\omega_p$  as a function of the initial radial distance to the center of the post  $r_0$  in Fig. 3(a) and also as a function of the reduced velocity  $\tilde{u}$  in Fig. 3(b). The range of  $\tilde{u}$  corresponds to typical experimental conditions ( $\zeta$  of the order of tens of mV,  $E_0 \approx 10$  kV/m, and  $\omega$  ranging from 10 to 100 rad/s). A good agreement is found for low drift velocity conditions, i.e., positions far from the pillar and/or high electric field frequency, in which  $\tilde{u} \ll 1$ . However, deviations from the analytical solution are found if, for example,  $\tilde{u} \leq 0.5$  for  $r_0 = 2$ .

### III. EXPERIMENTS

In order to experimentally validate the description given above for a TWE rotating around an insulating cylinder a simple 4-electrode device was constructed. A quadrupolar array of planar platinum microelectrodes was integrated within a microfluidic channel, as shown in Fig. 4(a). A 20  $\mu\text{m}$  diameter post was placed in the central position between the electrodes [see Fig. 4(b)]. These channels were fabricated from PDMS using standard soft lithography. The channels are 37  $\mu\text{m}$  high and the width of each arm is 200  $\mu\text{m}$ .

Experiments were performed with a KCl electrolyte at three different conductivities:  $\sigma = 1.5$  mS/m, 3 mS/m, and 6 mS/m seeded with 500 nm polystyrene fluorescent particles to act as fluid tracers. The PDMS channels were bonded to the glass substrate (with electrodes) using  $\text{O}_2$  plasma bonding. Prior to experiments, devices were primed with a surfactant solution [0.1% (w/v) Pluronic F-127] for at least 30 minutes

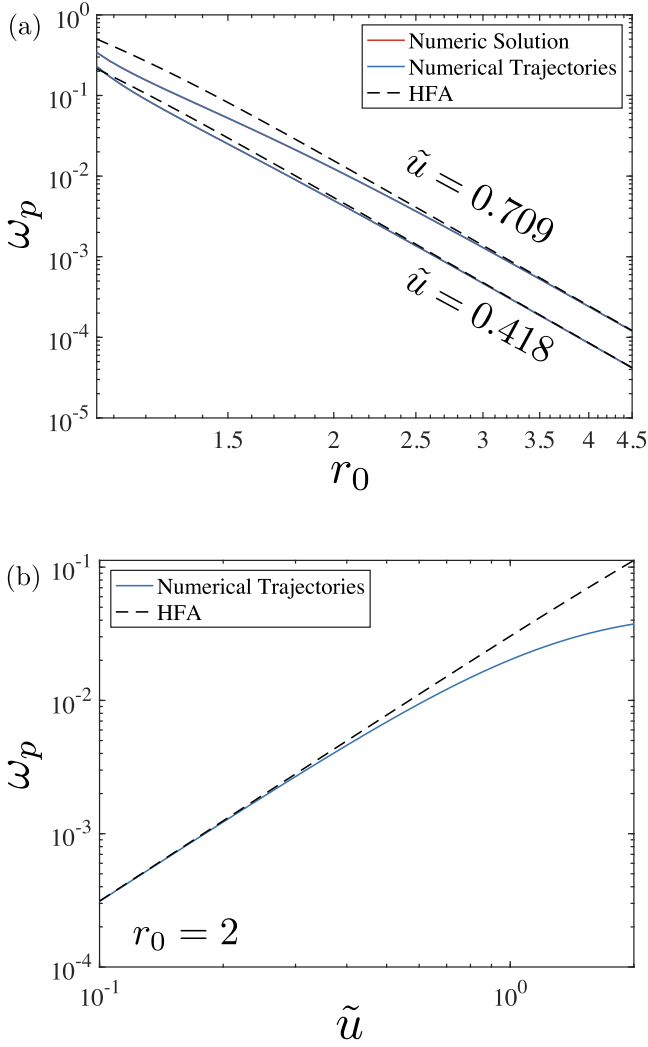


FIG. 3. Dependence of the drift angular velocity  $\omega_p$  on (a) the initial radius  $r_0$  and (b) the reduced velocity  $\tilde{u}$  given by direct numerical integration (solid curves) and HFA approximation (dashed lines). The reduced velocity  $\tilde{u} = 0.418$  shown in (a) represents the conditions for the particle trajectory plotted in Fig. 2(a) at  $r_0 = 2$ . Typical experimental parameters are  $\zeta = -63$  mV and  $E_0 = 10$  kV/m.

in order to avoid particle clogging and adhesion to channel walls.

The fluid is introduced in the channel through two reservoirs located at both ends of the channel, as seen in Fig. 4(a). Both reservoir inlets were connected to a pressure controller to control the fluid flow and eventually stop it to perform the rotation TWE experiments. Each of the four electrodes is connected to a signal generator which provides a sinusoidal signal of 10 Volts peak-to-peak, with frequencies ranging from 10 Hz to 100 Hz and a  $90^\circ$  phase delay between contiguous electrodes to produce the rotating field.

To analyze the flow, videos containing approximately 1000 frames were recorded and processed using particle image velocimetry (PIV) software [11]. Frames are taken at a constant rate of 16 fps, which is lower or of the order of the electric field frequency and, therefore, of the electrophoretic rotation. For that reason, tracer particles describe a full loop in each

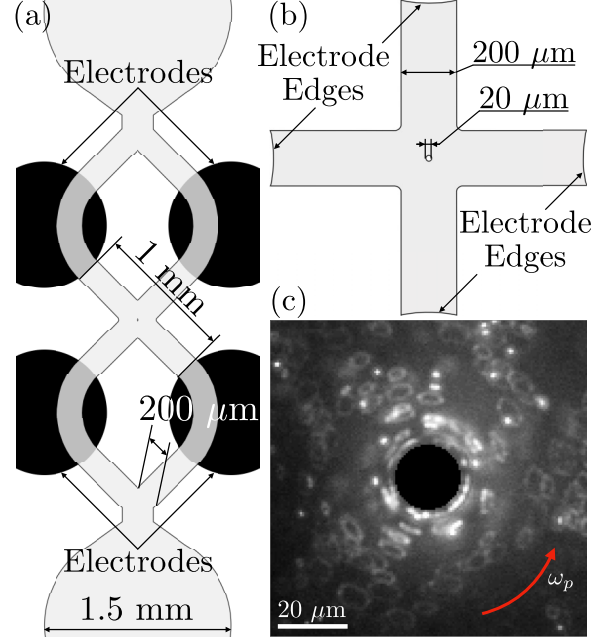


FIG. 4. Experimental setup for observing Rotating TWE (a) Top view of the microfluidic channel and the electrodes with the pillar in the center. (b) Detail of the channel showing the pillar. (c) Frame from one of the recordings showing the flow around the pillar ( $\sigma = 1.5$  mS/m,  $E_0 = 10$  kV/m,  $f = 17$  Hz).

frame for most cases, as shown in Fig. 4(c). Far from the pillar, loops are approximately circular allowing an estimate of the experimental mobility based on a linear regression from amplitude  $\mathcal{A}$  measurements at different frequencies; where  $\mathcal{A} = 2|\mu|E_0/\omega$ . For the case of the lowest conductivity of 1.5 mS/m, the mobility  $|\mu| = 4.35 \times 10^{-8}$  m<sup>2</sup>/(Vs); zeta-potential measurements of the tracer particles gives a similar value with  $|\mu| = \varepsilon|\zeta|/\eta = 4.46 \times 10^{-8}$  m<sup>2</sup>/(Vs). From the PIV measurements, the center of the loops was traced, giving an estimate of the drift angular velocity  $\omega_p$ .

Figure 5(a) shows PIV analysis of the experimental videos for an applied voltage with a frequency of 17 Hz ( $\tilde{u} = 0.418$ ), as a function of the distance to the post. Figure 5(b) shows data for a frequency sweep and an initial separation of  $r_0 = 2R$  from the surface of the post. The reduced mobilities in this case range from  $\tilde{u} = 0.154$  to 0.546. It was not possible to obtain reliable measurements for distances to the surface of the post for less than 5  $\mu\text{m}$  because it was not possible to trace the loops with the PIV software.

#### IV. COMPARISON BETWEEN THEORY AND EXPERIMENTS

Figure 5 shows experimental data for  $f = 17$  Hz together with the predictions of the theoretical model for  $\tilde{u} = 0.418$ , which corresponds to the expected reduced velocity for that frequency. There is a clear mismatch between theory and experiment, not only in the magnitude of  $\omega_p$ , but also in the trend with distance to the cylinder. This indicates there are contributions to the motion of the particles that are omitted. For this reason, we will now analyze the influence of the following on the particle trajectories: (i) The difference between the electric

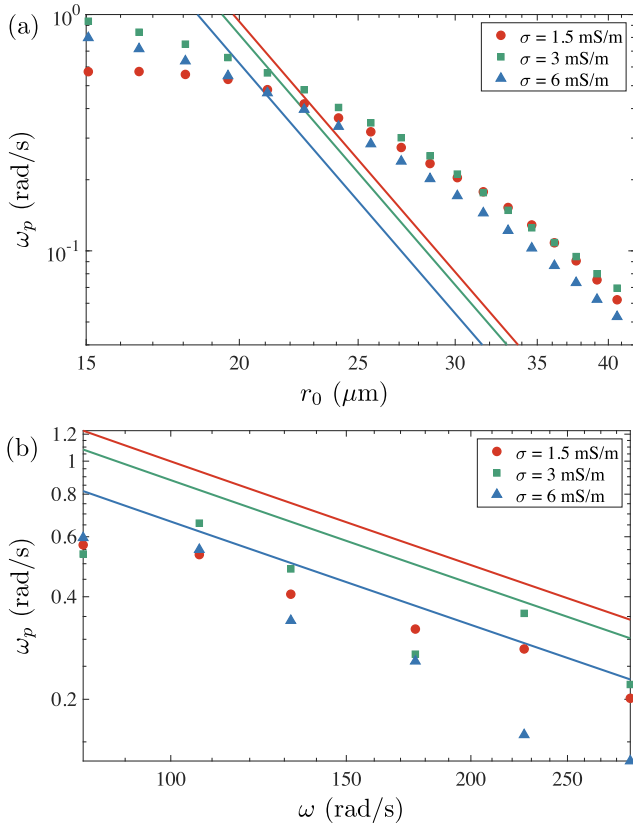


FIG. 5. PIV measurements determined from the experimental results. (a) Drift velocity  $\omega_p$  as a function of the radial distance to the center of the post for an electric field frequency of  $f = 17$  Hz, i.e.,  $\bar{u} = 0.418$  (b) Drift for a fixed distance to the post of  $r_0 = 2R$  as a function of the frequency, with reduced mobilities ranging from  $\bar{u} = 0.154$  ( $f = 46$  Hz) to  $\bar{u} = 0.546$  ( $f = 13$  Hz). Solid lines represent predictions from the HFA approximation given by Eq. (12).

field described so far and the electric field generated by the four electrodes and (ii) the contribution to particle rotation from the electro-osmosis generated on the channel walls.

### A. Electric field in the device

In order to accurately determine the electric field in the experimental device, the electric potential was calculated numerically in the 2D domain of Fig. 4(b) with the commercial software COMSOL Multiphysics. The electric potential is written as  $\phi(\mathbf{r}, t) = \phi_0(r, \theta) \cos(\omega t)$ , where  $\phi_0(r, \theta)$  is the solution of the Laplace equation ( $\nabla^2 \phi_0 = 0$ ) with the following boundary conditions: Zero current on the surface of the post and the channel walls ( $\mathbf{n} \cdot \nabla \phi_0|_S = 0$ ),  $\phi_0 = 0$  on the upper and lower electrodes,  $\phi_0 = 1$  on the left electrode and  $\phi_0 = -1$  on the right electrode.

Figure 6 shows the value of  $\phi_0$  along a circumference of radius  $r_0 = \sqrt{2} \times 200^2 / (2R)$  with its center on the post axis; this is the largest circumference concentric with the pillar allowed by the geometry. For comparison, we also show the electric potential calculated with Eq. (4) at  $t = 0$ . The difference between the maxima of the two curves is around 30%, which suggests that a more realistic simulation of the particle

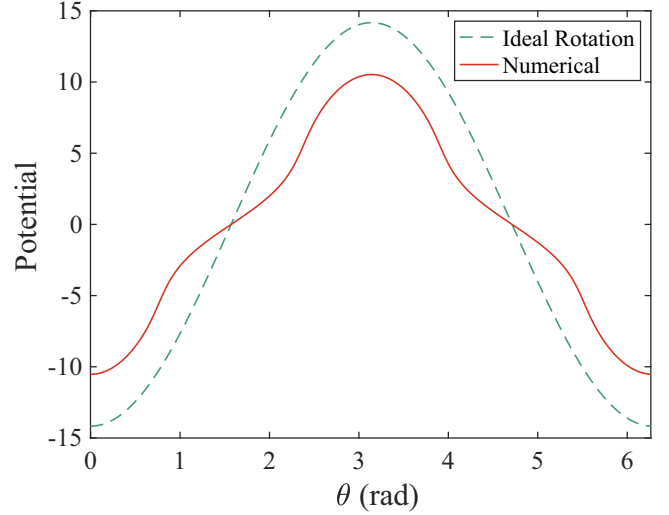


FIG. 6. Electric potential for the ideal rotating field (dashed green) and the numerical simulation (solid red) for the largest concentric circumference allowed by our geometry.

trajectories might require the exact numerical solution of the electric field in order to calculate the electrophoretic velocity. Simulations were also performed with COMSOL confirming that the trajectories of the particles are different for both situations. For example, Fig. 7 shows the trajectories of particles at several initial distances from the post for the ideal electric field [Eq. (5), red circles] and for the numerically calculated electric field (green circles). The arrows in that figure show the direction of the net particle motion (i.e., particle drift). Remarkably, the latter case shows that particles beyond a critical distance reverse their net motion; this never occurs with the ideal electric field. This finding motivated us to perform an analysis of the contributions to the particle motion of the angular modes of the electric field in the experimental device (see Appendix A).

Although reversal of particle motion was observed in experiments, the results of the simulations using the numerically calculated field do not agree with the measured dependence on radial distance. In particular, the simulations predict the crossover for the particle direction at a different radial position, i.e., the radius from the post at which the particle trajectory changes direction. This implies that there is some other mechanism missing in the analysis of particle velocity.

### B. Electro-osmosis in the channel

Recent publications have shown that the use of Pluronic drastically reduces the electro-osmotic mobility of the walls [12,13]. However, the residual electro-osmotic flow induced on the channel walls might still contribute to the particle motion. In this section we describe simulations of particle trajectories including the drag on the particles due to the electro-osmotic flow in the device.

Prior to the simulation of the trajectories, a numerical solution to the velocity field in the device is required. For this purpose, the Stokes equations ( $\nabla p = \eta \nabla^2 \mathbf{u}$  and  $\nabla \cdot \mathbf{u} = 0$ ) for the fluid velocity was included in the COMSOL model. Boundary conditions of electro-osmotic slip velocity ( $\mathbf{u} = -\varepsilon \zeta_w \mathbf{E} / \eta$ ) on the channel and post walls were used. In

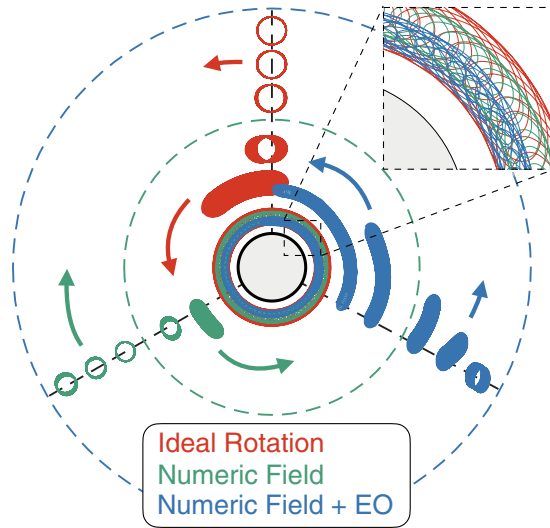


FIG. 7. Representation of the particle drift displacement after a fixed timespan ( $\omega t = 500$ ) as predicted by the different approaches. Red: Ideal rotation with drift velocity following Eq. (12). Green: Trajectories determined from the numerically calculated electric field. Blue: Numerically calculated trajectories given by the numerical field with the electro-osmotic back pressure. The green concentric circle describes the crossover radius of zero drift velocity in the simulation with the numeric electric field  $r_C = 4.37$ . The blue circumference represents the crossover radius found with the combination of the numeric field and electro-osmotic flow  $r_C = 7.66$ , which reproduces the experimental crossover radius (see Supplemental Material, movie [14]). These trajectories were computed for a typical experimental condition  $\sigma = 6$  mS/m,  $f = 17$  Hz ( $\tilde{u} = 0.418$ ). The top right inset image shows a closer view of the particle trajectories.

addition, a no flow conditions  $\mathbf{u} = 0$  was set on the electrode boundaries. To compute the electro-osmotic mobility, the zeta potential was set  $\zeta_w = -25$  mV, as determined from previous measurements of surfactant-treated PDMS [13].

### C. Comparison with experimental results

Figure 7 shows simulations of particle trajectories for the original description of the ideal rotation (Sec. II) along with the two major corrections presented above. The trajectory in red is the ideal condition where rotation is driven by the field given by Eq. (5) at different initial separation distances. Plotted in green are the trajectories of particles when using the numerically calculated field, and in blue the trajectories are for particles undergoing electrophoresis together with a drag force from the electro-osmotic flow created by the channel walls, with the electric field and fluid velocity field numerically computed.

All particle trajectories are computed for a fixed amount of time ( $t = 500$ ) in order to illustrate the dependence of velocity with initial separation from the post, for three different models. Simulations were made for typical experimental conditions: A conductivity of 6 mS/m, an electric field of magnitude  $E_0 = 10$  kV/m, and frequency of  $f = 17$  Hz, giving a reduced velocity of  $\tilde{u} = 0.418$ . The concentric dashed circumferences represent the radius of zero drift velocity predicted by the numerical electric field (green circumference),

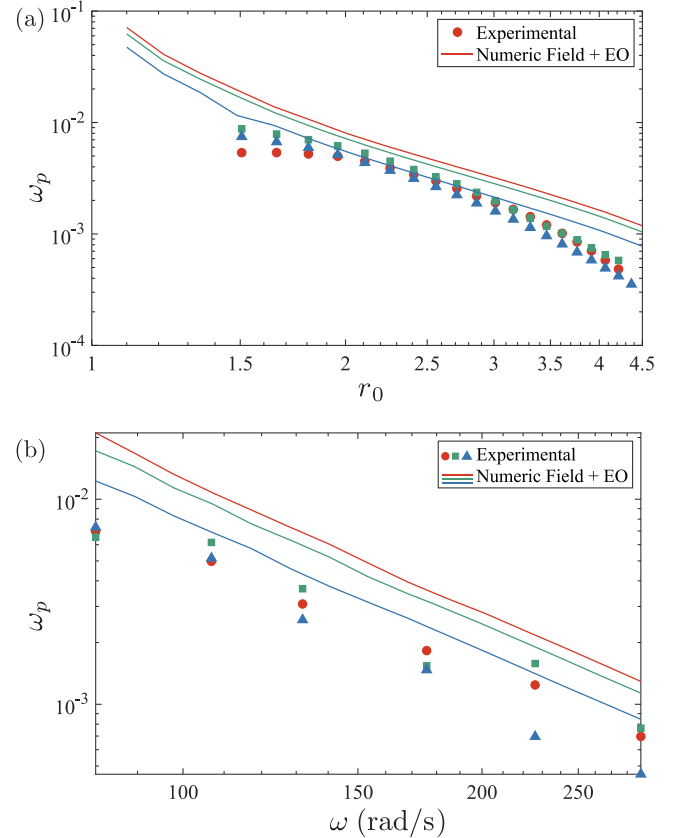


FIG. 8. Comparison between the experimental results and the numerically calculated trajectories when including the numerical electric field and the electroosmotic flow (solid lines). The plots show the drift velocity as a function of (a) the distance to the post for a fixed electric field frequency of  $f = 17$  Hz and (b) the frequency for a fixed distance to the post  $r_0 = 2R$ . Data is plotted for different conductivities: 1.5 mS/m (red), 3 mS/m (green) and 6 mS/m (blue). Data for zeta potential was determined from the experimental results in [13,15] and the Gouy-Chapman equation when needed for an extrapolation to different conductivities.

and the crossover radius predicted by a combination of numerical electric field and electro-osmotic flow (blue). Note that the amplitude of the loops described by the particles resemble the experimental conditions for the green and blue trajectories, but only the complete numerical approach (blue) describes the radial dependence of drift velocity that realistically describes the change in direction at  $r_C^{\text{Num}} = 7.66$ . The Supplemental Material movie [14] shows the change in the drift velocity at this radial for this distance.

Finally, Fig. 8 shows a comparison between the experimental drift velocities obtained by PIV measurements of the video recordings and the results from the numerical simulations obtained by averaging the angular displacement of particle trajectories such as those shown in Fig. 7 (blue). Figure 8(a) shows results for an electric field amplitude  $E_0 = 10$  kV/m and frequency  $f = 17$  Hz, for all experimental conductivities, as a function of distance to the center of the post. This shows that the numerically calculated electric field and fluid flow field ultimately results in a better description of the dependence of  $\omega_p$  with  $r$ . Figure 8(b) shows a frequency

sweep between 13 Hz and 46 Hz for a fixed initial radius at  $r_0 = 2R$  and the same electric field amplitude  $E_0 = 10$  kV/m. The comparison shows that the dependence with frequency is well predicted by the model.

To summarize for the TWE, the inclusion of the corrections presented above provide an explanation of both the magnitude of the observed drift velocity and the trend with frequency and distance to the pillar.

Thus, our model predicts that this system would allow fractionation of a sample mixture based on electrical mobility (zeta potential). Particles starting at a certain position drift around the post at different rates depending on mobility. The fact that the effect of electro-osmosis on the particles becomes dominant far from the post, where the TWE-induced angular drift velocity vanishes, means that the fractionation capabilities are most apparent in the vicinity of the pillar.

## V. CONCLUSIONS

We have demonstrated that the disturbance in a rotating field caused by the presence of a dielectric cylinder produces a traveling wave around the obstacle. This phenomenon occurs because of the presence of the dielectric object in the system, therefore we term it insulating traveling-wave electrophoresis (iTWE), analogous to the phenomenon of insulator-based dielectrophoresis (iDEP) [16–18].

A simple two-dimensional extension of the published TWE theory provides a qualitative description of the time-averaged drift velocity that matches the observed dependence with frequency of applied electric field and the decay with the distance from the post. A more detailed description of the experimental geometry that takes into account the electro-osmotic flows generated in the channels provides a good agreement with the experimental observations.

Additional effects such as electrothermal flows can be discounted since the frequency-dependent behavior is not the same, and the light illumination did not influence the experimental observations [19]. Furthermore, the frequencies of the ac voltages are too low to cause traveling-wave dielectrophoresis (twDEP) [20].

The observed phenomenon provides a new way for manipulation of colloidal particles far from the electrodes—a major problem in the field of microfluidics and electrokinetics, as discussed in the introduction. An optimized geometry that exploits these fundamental forces could be used to fractionate a suspension of particles based on different mobilities.

The data that support the findings of this study are openly accessible in the University of Southampton repository available in Ref. [21].

## ACKNOWLEDGMENT

P.G.S. and A.R. acknowledge Grant No. P20\_00534 funded by “Consejería de Economía, Conocimiento, Empresas y Universidad (Junta de Andalucía)”.

## APPENDIX A: ELECTRIC FIELD ANALYSIS

In order to understand the effect of the experimental electric field on particle trajectories, an analytical expression for

the electric potential in the neighborhood of the pillars is required. This was performed based on separation of variables in polar cylindrical coordinates. First write a general solution for the potential at time  $t = 0$  that satisfies the boundary condition on the pillar surface ( $\mathbf{n} \cdot \nabla \phi|_S = 0$  at  $r = 1$ ), while preserving the vertical and horizontal symmetry axes of the geometry [see Fig. 4(b)]

$$\phi^M(r, \theta) = \sum_{n=0}^{\infty} A_n \left( r^{2n+1} + \frac{1}{r^{2n+1}} \right) \cos[(2n+1)\theta]. \quad (\text{A1})$$

Note that  $n = 0$  represents the ideal electric potential, the most relevant contribution.

To obtain the coefficients  $A_n$ , we equate the series expansion to the numerical solution of the potential at a certain radius  $r_{\text{comp}}$  far from the post. We choose  $r_{\text{comp}} = \sqrt{2 \times 200^2} / (2R)$ . The first two coefficients are found to be  $A_0 = -0.6452$  and  $A_1 = -6.077 \times 10^{-4}$ . With only these two modes,  $\phi^M$  differs from the numerically calculated potential by less than 3%.

We now proceed to write the full time-dependent electrical potential. The experimental electric field is generated by two sinusoidal ac signals which are out of phase by 90 degrees and are applied to two pairs of electrodes rotated by 90 degrees. That is, the time-dependent potential can be expressed as

$$\begin{aligned} \phi(r, \theta, t) &= \phi^M(r, \theta) \cos t + \phi^M(r, \theta - \pi/2) \sin t \\ &= \sum_{n=0}^{\infty} A_n \left( r^{2n+1} + \frac{1}{r^{2n+1}} \right) \left( \cos[(2n+1)\theta] \cos t \right. \\ &\quad \left. + \cos \left[ (2n+1) \left( \theta - \frac{\pi}{2} \right) \right] \sin t \right). \end{aligned} \quad (\text{A2})$$

Using the identity  $\cos[(2n+1)(\theta - \pi/2)] = (-1)^n \sin[(2n+1)\theta]$ , the above expression can be rewritten as

$$\phi = \sum_{n=0}^{\infty} A_n \left( r^{2n+1} + \frac{1}{r^{2n+1}} \right) \cos[(2n+1)\theta - (-1)^n t]. \quad (\text{A3})$$

This shows that the potential is the superposition of modes rotating alternately clockwise or anticlockwise depending on whether  $n$  is odd or even, respectively. This is the origin of the reversal in the drift velocity with radius shown in Fig. 7 when the rotation is calculated from the numerical field.

Using the HFA method, we now arrive at an analytical expression for the particle drift angular velocity  $\omega_p$ :

$$\omega_p = \frac{\sum_n (-1)^n (2n+1) G_n}{2/\bar{u}^2 - \sum_n (2n+1)^2 G_n}, \quad (\text{A4})$$

where  $G_n$  are radial functions for each mode. This expression and the first modes are derived in Appendix B. Interestingly, the expression predicts a change of sign in drift angular velocity as a function of  $r$ . Using just the first two modes of the potential  $n = 0, 1$  in Eq. (A4) and with  $G_0$  and  $G_1$  shown in Eqs. (B11) and (B12), respectively, the crossover radius  $r_C$  of zero drift velocity is given by

$$r_C \approx \left( \frac{A_0}{3A_1} \right)^{1/4} \approx 4.37. \quad (\text{A5})$$

### APPENDIX B: HFA APPROXIMATION FOR THE COMPLETE ELECTRICAL PROBLEM

We write the expression Eq. (A3) as

$$\phi(r, \theta, t) = \sum_{n=0}^{\infty} F_n(r) \cos[k_n \theta - (-1)^n t]. \quad (\text{B1})$$

The equations for particle motion become

$$\frac{dr}{dt} = -\tilde{u} \sum_{n=0}^{\infty} f_n(r) \cos[k_n \theta - (-1)^n t], \quad (\text{B2})$$

$$\frac{d\theta}{dt} = \tilde{u} \sum_{n=0}^{\infty} k_n \frac{F_n(r)}{r^2} \sin[k_n \theta - (-1)^n t], \quad (\text{B3})$$

where we define  $f_n(r) = F'_n(r)$ . As in Eq. (6), Sec. II, we write  $r$  and  $\theta$  as the sum of time-averaged and oscillating components, leading to

$$\begin{aligned} \frac{dr'}{dt} &= -\tilde{u} \sum_{n=0}^{\infty} f_n(r' + r_0) \cos(k_n \theta' - \Omega_n t), \\ \omega_p + \frac{d\theta'}{dt} &= \tilde{u} \sum_{n=0}^{\infty} k_n \frac{F_n(r' + r_0)}{(r' + r_0)^2} \sin(k_n \theta' - \Omega_n t), \end{aligned}$$

where we define  $\Omega_n = (-1)^n - k_n \omega_p$ . Suppose now that  $r', \theta' \ll 1$ , meaning that to first order we can write

$$\begin{aligned} \frac{dr'}{dt} &= -\tilde{u} \sum_{n=0}^{\infty} [f_n(r_0) \cos(\Omega_n t) + f'_n(r_0) \cos(\Omega_n t) r' \\ &\quad + k_n f_n(r_0) \sin(\Omega_n t) \theta' + \dots], \end{aligned} \quad (\text{B4})$$

$$\begin{aligned} \omega_p + \frac{d\theta'}{dt} &= \tilde{u} \sum_{n=0}^{\infty} k_n \left[ -\frac{F_n(r_0)}{r_0^2} \sin(\Omega_n t) \right. \\ &\quad - \left( \frac{f_n(r_0)}{r_0^2} - \frac{2F_n(r_0)}{r_0^3} \right) \sin(\Omega_n t) r' \\ &\quad \left. + k_n \frac{F_n(r_0)}{r_0^2} \cos(\Omega_n t) \theta' + \dots \right]. \end{aligned} \quad (\text{B5})$$

It can be observed from the above equations that the oscillating functions not only have the frequency modes  $\{\Omega_n\}$ ,  $n \in \{0, \mathbb{N}\}$  but also cross terms with frequencies  $\{|\Omega_i \pm \Omega_j|\}$ ,  $i \neq j \in \{0, \mathbb{N}\}$ . However, as we are only interested in the time-averaged part of Eq. (B5), then only the first terms (and not all of them) in Eq. (B4) and the oscillating part of Eq. (B5) survive:

$$\frac{dr'}{dt} = -\tilde{u} \sum_{n=0}^{\infty} f_n(r_0) \cos(\Omega_n t), \quad (\text{B6})$$

$$\frac{d\theta'}{dt} = -\tilde{u} \sum_{n=0}^{\infty} k_n \frac{F_n(r_0)}{r_0^2} \sin(\Omega_n t). \quad (\text{B7})$$

These can be readily integrated and substituted into Eq. (B5). Taking the time average yields terms of the form

$$\langle \sin(\Omega_n t) \sin(\Omega_m t) \rangle = \frac{\delta_{n,m}}{2}, \quad \langle \cos(\Omega_n t) \cos(\Omega_l t) \rangle = \frac{\delta_{n,l}}{2},$$

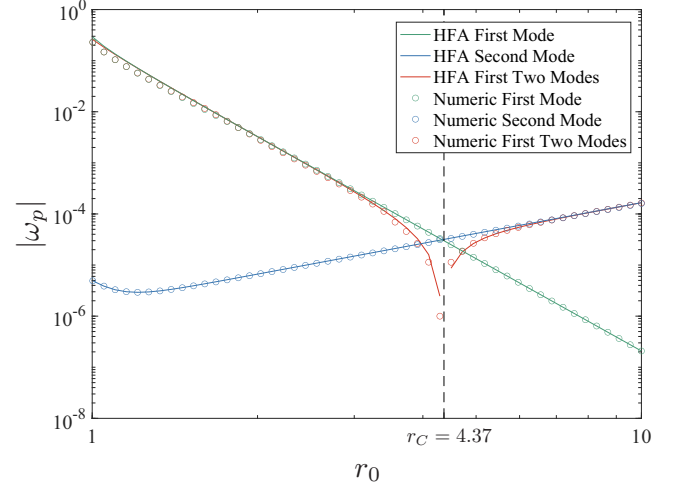


FIG. 9. Comparison between the HFA approximation results and direct numerical simulations of particle trajectories. Drift velocities corresponding to the first and second modes are shown in green and blue, respectively. The combination of the first two modes is represented in red, where the reversal in velocity can be observed at  $r_C$ .  $A_0 = -0.6452$ ,  $A_1 = -6.077 \times 10^{-4}$ ,  $\tilde{u} = 0.5$ .

where  $\delta_{i,j}$  is the Kronecker delta, whose value is 1 if  $i = j$  and 0 otherwise. We can finally write

$$\begin{aligned} \omega_p &= \frac{\tilde{u}^2}{2R^2} \sum_{n=0}^{\infty} \frac{k_n}{\Omega_n} \\ &\quad \times \left[ f_n^2(r_0) - \frac{2}{r_0} F_n(r_0) f_n(r_0) + \frac{k_n^2}{r_0^2} F_n^2(r_0) \right]. \end{aligned} \quad (\text{B8})$$

Defining the generatrix function

$$\begin{aligned} G_j &= G\{F_j(r_0)\} \\ &= \frac{1}{r_0^2} \left[ f_j^2(r_0) - \frac{2}{r_0} F_j(r_0) f_j(r_0) + \frac{k_j^2}{r_0^2} F_j^2(r_0) \right] \end{aligned} \quad (\text{B9})$$

and noting that  $\Omega_n = (-1)^n - k_n \omega_p$ , we can express the drift velocity in the limit  $\omega_p \ll 1$  as

$$\omega_p = \frac{\sum_n (-1)^n k_n G_n}{2/\tilde{u}^2 - \sum_n k_n^2 G_n}, \quad (\text{B10})$$

which is the equation presented in Eq. (A4).

For the first two modes we have

$$F_0(r) = A_0 \left( r + \frac{1}{r} \right), \quad F_1(r) = A_1 \left( r^3 + \frac{1}{r^3} \right),$$

together with  $k_0 = 1$  and  $k_1 = 3$ , so that

$$G\{F_0(r_0)\} = \frac{4A_0^2}{r_0^6}, \quad (\text{B11})$$

$$G\{F_1(r_0)\} = 12A_1^2 \left[ \frac{2}{r_0^{10}} + r_0^2 \right]. \quad (\text{B12})$$

To test the validity of the average drift velocity obtained from the HFA approximation, Fig. 9 compares the resulting  $\omega_p$  with the numerical simulations for the same electric field, using the first two modes. The absolute value is used to allow comparison with the second mode.

- [1] J. W. Jorgenson and K. D. Lukacs, *Science* **222**, 266 (1983).
- [2] R. Hunter, *Introduction to Modern Colloid Science* (Oxford University Press, New York, 1993).
- [3] M. von Smoluchowski, *Bull. Akad. Sci. Cracovie.* **8**, 182 (1903).
- [4] B. F. Edwards, A. T. Timperman, R. L. Carroll, K. Jo, J. M. Mease, and J. E. Schiffbauer, *Phys. Rev. Lett.* **102**, 076103 (2009).
- [5] H.-H. Wei, *Appl. Phys. Lett.* **90**, 204103 (2007).
- [6] K. D. Jo, J. E. Schiffbauer, B. E. Edwards, R. L. Carroll, and A. T. Timperman, *Analyst* **137**, 875 (2012).
- [7] P. García-Sánchez, A. Ramos, A. González, N. G. Green, and H. Morgan, *Langmuir* **25**, 4988 (2009).
- [8] A. Ramos, A. González, P. García-Sánchez, and A. Castellanos, *J. Colloid Interface Sci.* **309**, 323 (2007).
- [9] A. S. Khair, *Curr. Opin. Colloid Interface Sci.* **59**, 101587 (2022).
- [10] J. R. Melcher, E. Warren, and R. H. Kotwal, *Part. Sci. Technol.* **7**, 1 (1989).
- [11] W. Thielicke and E. J. Stamhuis, *J. Open Res. Softw.* **2**, 30 (2014).
- [12] M. Viefhues, S. Manchanda, T.-C. Chao, D. Anselmetti, J. Regtmeier, and A. Ros, *Anal. Bioanal. Chem.* **401**, 2113 (2011).
- [13] R. Fernández-Mateo, P. García-Sánchez, V. Calero, A. Ramos, and H. Morgan, *Electrophoresis* **43**, 1259 (2022).
- [14] See Supplemental Material at <http://link.aps.org/supplemental/10.1103/PhysRevE.108.015104>, which contains a video showing particles undergoing iTWE around a microfluidic pillar when a 10 kV/m, 21 Hz rotating field is applied.
- [15] V. Calero, P. Garcia-Sanchez, A. Ramos, and H. Morgan, *Biomicrofluidics* **13**, 054110 (2019).
- [16] B. H. Lapizco-Encinas, B. A. Simmons, E. B. Cummings, and Y. Fintschenko, *Anal. Chem.* **76**, 1571 (2004).
- [17] N. Hill and B. H. Lapizco-Encinas, *Electrophoresis* **40**, 2541 (2019).
- [18] B. H. Lapizco-Encinas, *Anal. Bioanal. Chem.* **414**, 885 (2022).
- [19] A. González, A. Ramos, H. Morgan, N. G. Green, and A. Castellanos, *J. Fluid Mech.* **564**, 415 (2006).
- [20] H. Morgan and N. G. Green, *AC Electrokinetics: Colloids and Nanoparticles* (Research Studies Press Ltd., Baldock, 2003).
- [21] <https://doi.org/10.5258/SOTON/D2699>.